



SMART analysis of geomagnetic data observed in Taiwan

C.H. Chen^a, J.Y. Liu^{b,c,*}, W.H. Yang^b, H.Y. Yen^d, K. Hattori^e, C.R. Lin^{a,d}, Y.H. Yeh^a

^a Institute of Earth Sciences, Academia Sinica, Taipei 115, Taiwan

^b Institute of Space Science, National Central University, Chung-Li 32054, Taiwan

^c Center for Space and Remote Sensing Research, National Central University, Chung-Li 32054, Taiwan

^d Institute of Geophysics, National Central University, Chung-Li 32054, Taiwan

^e Graduate School of Science, Chiba University, Inage, Chiba 263-8522, Japan

ARTICLE INFO

Article history:

Received 26 February 2008

Received in revised form 27 August 2008

Accepted 1 September 2008

Available online 12 September 2008

Keywords:

Earthquake prediction

Geomagnetic anomaly

Geomagnetic polarization

Singular value decomposition

ABSTRACT

In this paper, 3-component geomagnetic fields recorded by a fluxgate magnetometer are employed in examining 181 $ML \geq 4.0$ earthquakes around the Taiwan area from 2002 to 2005. To search anomalies, the singular value decomposition (SVD) is used to extract the declinations and inclinations of the principal components from the geomagnetic field every 900 s for each 5-day period and the entire four years. Six reference angles of surface magnetic anomaly reference tip (SMART) are employed to readjust the azimuth of anomalous polarizations for unifying earthquakes. A bootstrap method is further applied to find whether the anomalies are significant or not. Meanwhile, the odds proportions between the inward and outward geomagnetic field on the earth's surface reveal the associated anomalous inclinations. With the anomalous inclinations and declinations observed 10 days before earthquakes, SMART and the polarizations of the anomalous field can be located and described, respectively.

© 2008 Elsevier Ltd. All rights reserved.

Introduction

Geomagnetic anomalies associated with many earthquakes in a wide frequency range from DC to VLF have been reported in many studies (Hayakawa and Fujinawa, 1994; Hayakawa, 1999; Hayakawa and Molchanov, 2002). Based on convincing evidence observed during several major earthquakes, variations of geomagnetic anomalies within the ULF frequency range (≤ 300 Hz) are considered promisingly notable phenomena in anticipating earthquakes (Bernardi et al., 1991; Molchanov et al., 1992, 1995; Kopytenko et al., 1993; Hayakawa et al., 1999, 2000; Kawate et al., 1998; Gotoh et al., 2002; Hattori et al., 2002; Hattori, 2004). Using the Loma Prieta earthquake (M_s 7.1, October 17, 1989) as an example, a magnetic sensor located near the epicenter observed the intense anomalies suddenly increasing in one component few hours ago (Fraser-Smith et al., 1990). Yet, four years later, no anomalies were observed by magnetometers in the same area during Northridge earthquake (M 6.7, January 17, 1994) because the epicentral distance was too large (Fraser-Smith et al., 1994). Therefore, Hattori et al., 2004 summarized the experiences from many major earthquakes and suggested a relationship between the ULF anomalies and earthquakes in the form of the earthquake magnitude vs. the epicentral distance. Meanwhile, Hattori et al., 2004b also suggested that anomalous signals involved in the daily variation (Chapman and Bartels, 1940) were very weak because the

sensors were generally set far away from the epicenters. To identify weak anomalies, principal component analyses were employed in signal discrimination during the Izu Islands earthquake (Gotoh et al., 2002; Hattori, 2004, 2006). Telesca et al. (2004) and Telesca and Hattori (2007) also found that earthquake forecast patterns of the principal component approached seismic areas.

Otherwise, if an earthquake occurs with a surface rupture zone, locations of the fault generally have some distance away from its epicenter. Alternatively, Merzer and Klempner (1997) and Yen et al. (2004) suggested that the conductivity and/or current along a fault (or slip plane) disturbed nearby the geomagnetic field strengths during the earthquake preparation period. Chen et al. (submitted for publication) combine the ideas of the fault and the epicenter developing a hybrid system, the surface magnetic anomaly reference tip (SMART). In the SMART system, the fault and nodal planes are extended with their associated constant dips to intersect the earth's surface obtaining the fault and nodal lines. Based on the SMART system, six reference angles can be computed, and the distances from the station to the fault line, DF , and to the nodal line, DN , as well as their sum, $DT = (DF^2 + DN^2)^{1/2}$, are calculated (for detail see, Chen et al., 2008).

In this paper, the principal components of ULF magnetic signals in geomagnetic fields recorded by a 3-component fluxgate magnetometer station are derived and readjusted by the six reference angles of SMART. The readjusted principal components are further examined during 181 earthquakes ($ML \geq 4.0$ and $DT < 120$ km) in Taiwan during the four-year period of 2002–2005 (Fig. 1a).

* Corresponding author. Address: Institute of Space Science, National Central University, Chung-Li 32054, Taiwan. Tel.: +886 3 4228374; fax: +886 3 4224394.

E-mail address: jyliu@jupiter.ss.ncu.edu.tw (J.Y. Liu).

Model and methodology

Chapman and Bartels (1940) propose that the ionosphere and the telluric currents mainly affect variations of the geomagnetic field, while Balkey (1995) indicates that observed geomagnetic field could also result from the induction field due to susceptibilities of underground rocks. Based on these, the geomagnetic field survey on the ground is widely employed in investigating the magnetic structure underground (Hsieh and Hu, 1972; Bhattacharyya and Leu; 1975; Robert and Cain, 1975; Hu and Chen, 1986; Yen et al., in press). Meanwhile, the earthquake preparation is a long term process of accumulated and changed stress underground (Shearer, 1999), which in turn causes magnetic susceptibility changes (Kapicka et al., 2003). Although the exact mechanism is not fully understood, the geomagnetic anomalies have been observed during the earthquake preparation process.

Assume data daily recorded with 1 Hz resolution at the 3-component fluxgate magnetometer station to be given as, X_i, Y_i, Z_i , which monitor variations of the geomagnetic field involving effects of the ionosphere and the telluric currents as well as the rock susceptibilities. However, Chapman and Bartels (1940) find that the daily variation of the geomagnetic field, which is affected by both the ionosphere and the telluric currents, are generally similar every day. To remove the susceptibility effect, we then subtract the first data point of the day, X_1, Y_1, Z_1 , at 0:00LT (local time) from the daily recorded data to obtain an new offset data ($X_i - X_1, Y_i - Y_1, Z_i - Z_1, i = 1-86400$). We can further compute the principal components of asymmetric matrixes (900×3) by the original and offset data every 900 s during four-year period.

To extract and purify the principal component, the singular value decomposition (SVD) has been used (Jolliffe, 2002). With SVD, any $m \times n$ asymmetric matrix a can be given as the product of an

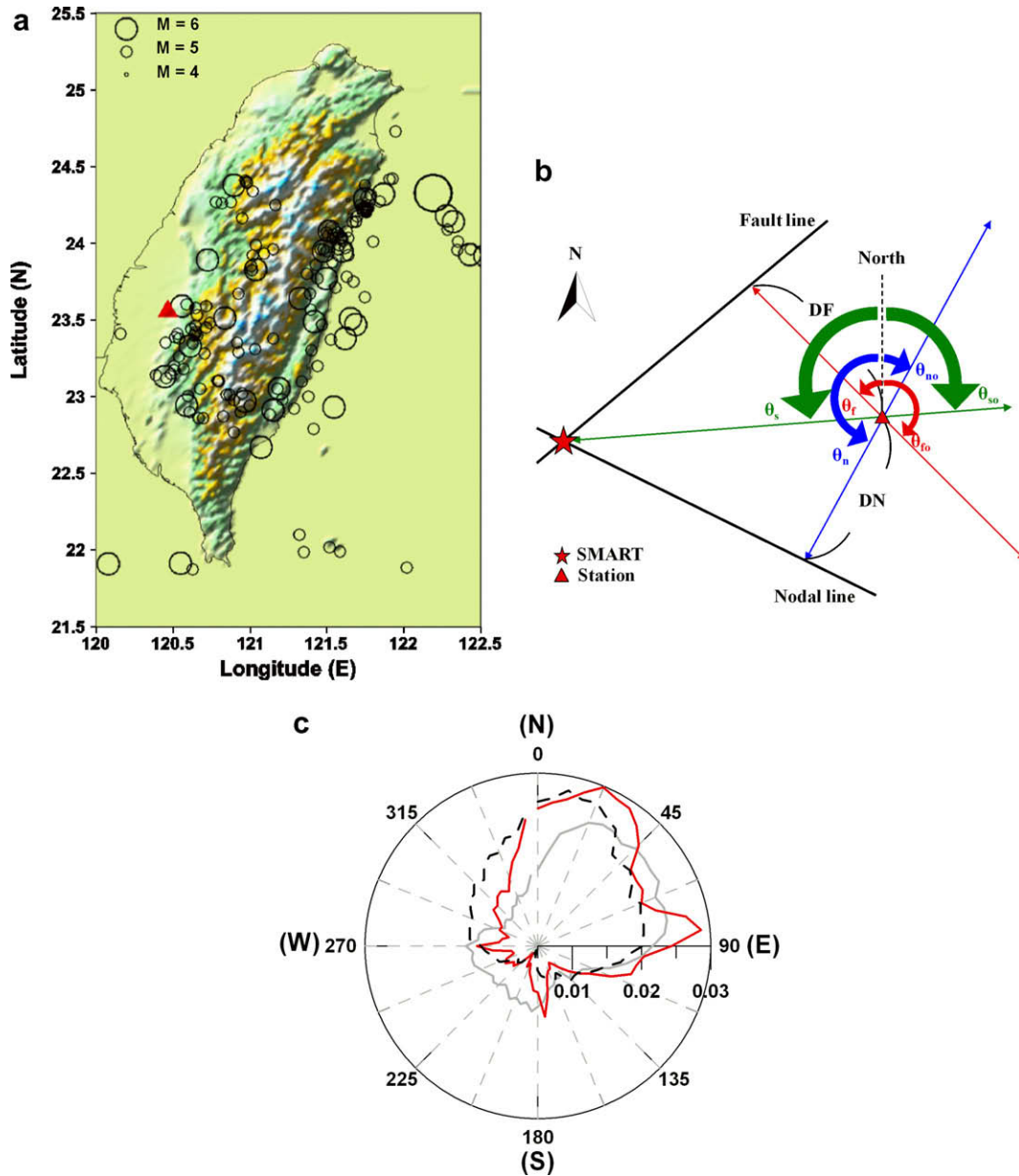


Fig. 1. The basic data reading the station, the earthquakes and background of the geomagnetic field. The \blacktriangle and \circ , respectively, show the locations of the station and the 181 earthquakes ($ML \geq 4$ and $DT < 120$ km), and the size of \circ also denotes the magnitude of earthquakes (a). The azimuth angles are determined by the fault line, nodal line and SMART in the SMART system (b). The distributions of θD_r (red line) and θD_m (black dash line) obtained by SVD are related to the azimuth (c). The radiuses indicate the normalized proportions at the associated azimuths. Moreover, the shallow line given by principal component analysis shows the normalized proportions are increase at the false azimuths. For interpretation of the references to colour in this figure legend, the reader is referred to the web version of this article.

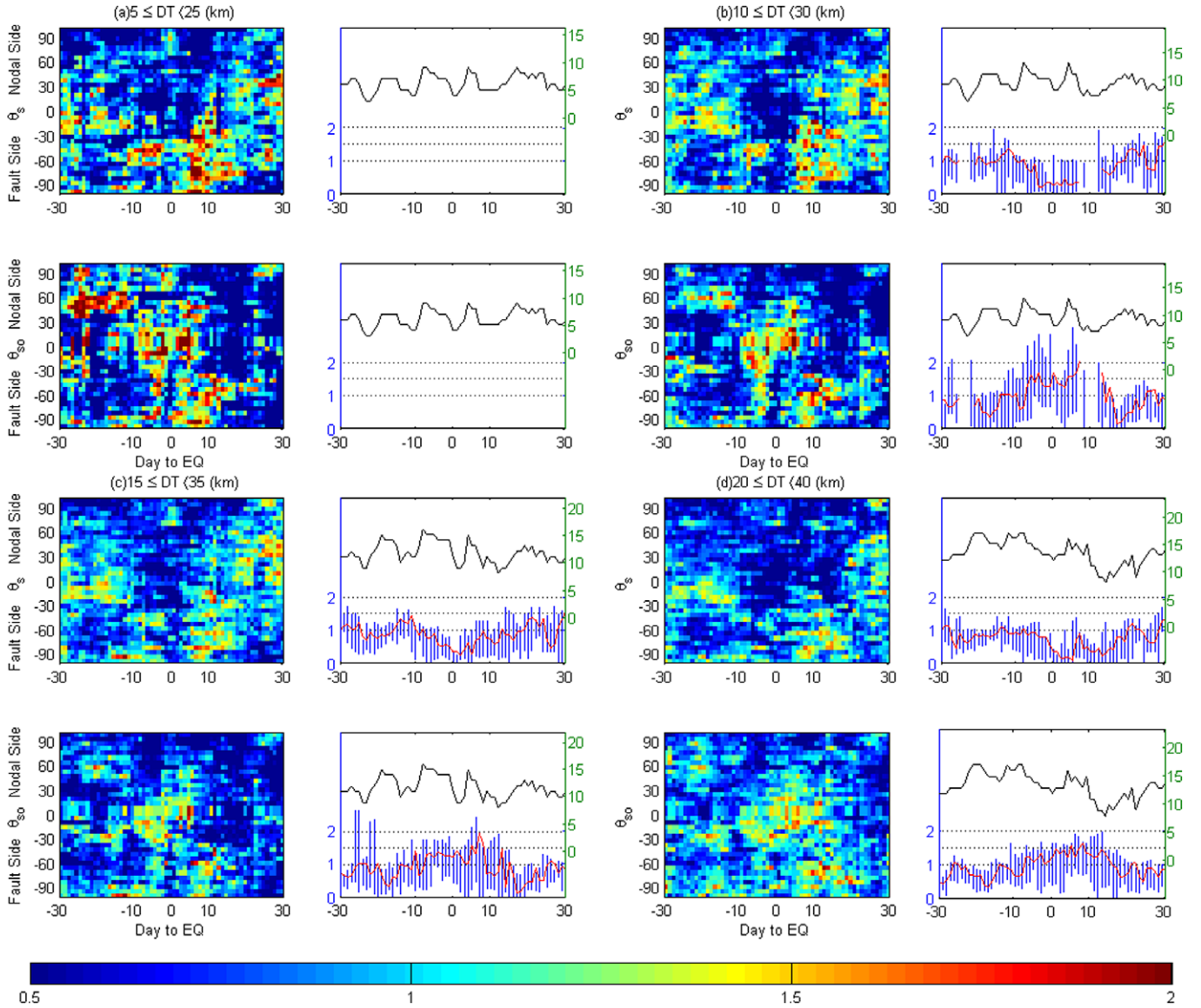


Fig. 2. The variations of P_{θ_s} and $P_{\theta_{so}}$, and the bootstrap results for the direction between SMART and the station 30 days before and after the earthquakes. The distance of DT from 0 to 80 km are denoted with (a–g), respectively. The left side of the upper and bottom panels in each diagram shows the P_{θ_s} and $P_{\theta_{so}}$ and the right sides of them are the bootstrap results at θ_s and θ_{so} . To determine the relationship between earthquakes and the polarization of geomagnetic fields at the station, the parameters are regulated to a sequence of north-fault-station-nodal for identification of the direction of the anomaly source. Therefore, the positive angles of P_{θ_s} and $P_{\theta_{so}}$, respectively, to θ_s and θ_{so} face the nodal side. Conversely, the negative part means that the polarization directs to the fault side. The red area shows that the geomagnetic azimuths gather at angles to θ_s/θ_{so} of the y-axis directions. With bootstrap analyses, the blue shadowed areas denote a range of 90% confidence intervals and the red line within the intervals is the median at the angle, θ_s/θ_{so} , (left y-axis). The black line shows the numbers of recorded events (right y-axis) and the x-axis indicates the days to the earthquakes. Due to few event occurrences within a range of $5 < DT < 25$ km, bootstrap results cannot be obtained (a). For interpretation of the references to colour in this figure legend, the reader is referred to the web version of this article.

$m \times n$ matrix u , an $n \times n$ diagonal matrix v with positive or zero elements, and an $n \times n$ matrix p , and written as $a = u \cdot v \cdot p^t$. Similarly, a transfer matrix $a^t = p \cdot v \cdot u^t$ can be obtained, where $u \cdot u^t = p \cdot p^t = 1$. The principal components then can be obtained by an $n \times n$ matrix $a^t \cdot a$

$$a^t \cdot a = p \cdot v \cdot u^t \cdot u \cdot v \cdot p^t = p \cdot v \cdot v \cdot p^t,$$

and

$$a^t \cdot a \cdot p = p \cdot v \cdot v \cdot p^t \cdot p = p \cdot v^2$$

where p is the eigenvectors and v^2 is the eigenvalues of the principal components. The most important principal component is the largest (first) eigenvalues and the declinations (Jolliffe, 2002), θD_r and θD_m are, respectively, given by the pairing first eigenvector for determin-

ing the background and monitor data. Here, based on the computed eigenvector, we calculate the azimuth distributions every 900 data points (seconds) of the offset data for the entire four-year period to construct the background (i.e. θD_r). Similarly, we compute azimuth distributions every 900 data points (seconds) of the original data for 5-day period to obtain the monitor (i.e. θD_m). Both the background and monitor azimuth distributions are binned each 2.5° and self-normalized. The normalized distribution of the monitor is further divided by that of the background to find the most significant changes from the background, which stands for the azimuth of pronounced anomalies (P_a) during each earthquake period. Here, the azimuth of P_a is based on the north direction. Note that if P_a approaches 1, the monitor is similar to the background which means no anomalies are detected.

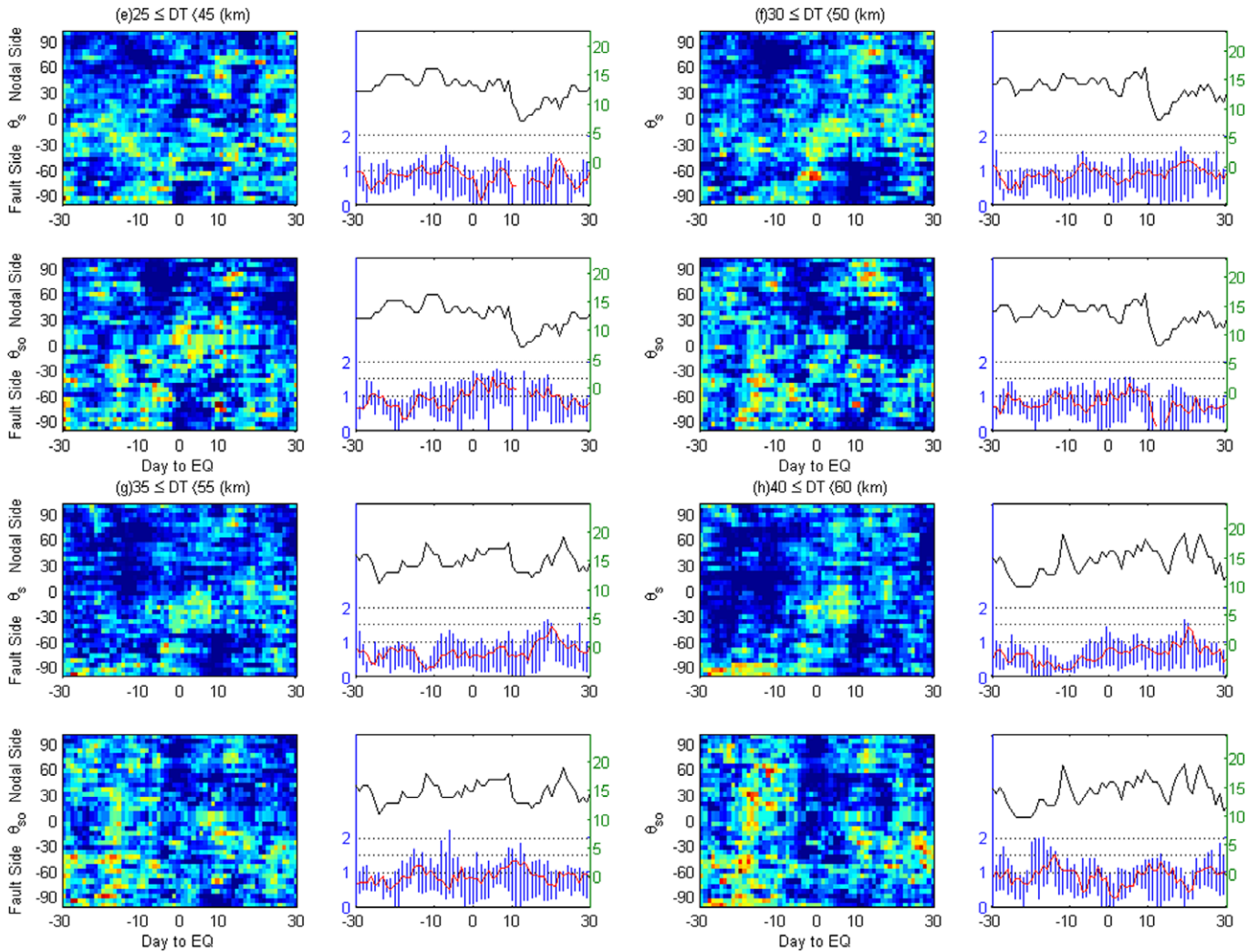


Fig. 2 (continued)

Each earthquake can be relocated by six angles of SMART. Three reference angles from the northward to the station–SMART line θ_s , to the direction toward the fault line θ_f , and to the direction toward the nodal line θ_n on the surface are computed to search the location of anomalies within the domain -90° – 90° (Fig. 1b). If θD_m equals to θ_s , θ_f , and/or θ_n , the geomagnetic field at the station should point to SMART, the fault line and/or nodal line, respectively. On the other hand, the other three reference angles from the northward to the anti SMART θ_{so} , to the direction away from the fault line θ_{fo} , and to the direction away from the nodal line θ_{no} are also calculated to find the location of anomalies within the other domain -90° – 90° (Fig. 1b). To unify all the earthquakes, P_a computed 30 days before and after each earthquake are readjusted by the six associated reference angles. For example, P_{θ_s} denotes that P_a vs. the northward direction has been readjusted (or transferred) to vs. the station–SMART direction (i.e. $P_{\theta_s} = P_a - \theta_s$). Similarly, the other five are readjusted as, $P_{\theta_{so}} = P_a - \theta_{so}$, $P_{\theta_f} = P_a - \theta_f$, $P_{\theta_{fo}} = P_a - \theta_{fo}$, $P_{\theta_n} = P_a - \theta_n$, and $P_{\theta_{no}} = P_a - \theta_{no}$. Note that P_{θ_f} (or $P_{\theta_{fo}}$) and P_{θ_n} (or $P_{\theta_{no}}$) are given by the earthquakes when $DF \leq 15$ km and $DN \leq 15$ km, respectively.

Moreover, to measure whether the six readjusted P_a are certainly larger than the background (one), bias-corrected and accelerated approach (Efron, 1987) is employed. The bias-corrected and accelerated approach is a bootstrap method which makes sta-

tistical inferences based on a collection of a large number of new sub-samples from the initial sample. Therefore, the method can provide more confident inferences than general statistical methods if the sample size is not sufficiently large. After 5000 bootstrap processes, a 90% confidence interval (90CI) will contain possible distribution range of the median of the P_a . Since effects of the geomagnetic field polarization during earthquake periods, 90CI does not contain 1 implying P_a mainly distribute at other polarizations. Otherwise, if the low bound of 90CIs are close or larger than 1, the anomalies at the examined reference azimuth are clearly evident within the background.

In addition, the inclinations of the first eigenvector are also taken into consideration. The earthquakes are sorted by DT for determining the inclinations, θI_m , nearby and away from SMART. Similarly, θI_m changed with DT along the fault and nodal lines are also obtained by the same analysis process for $DF \leq 15$ km and $DN \leq 15$ km, respectively. To examine that θI_m are significant/insignificant to the background, the odds test which is the quantity $p/(1-p)$, where p is the probability of success are employed (Agresti, 2002). With the odds larger than 1, a success is more likely than a failure. Inversely, a failure is more likely than a success. Then, we combine results of P_a and θI_m to describe the polarizations of the geomagnetic field related with SMART, the fault and nodal lines.

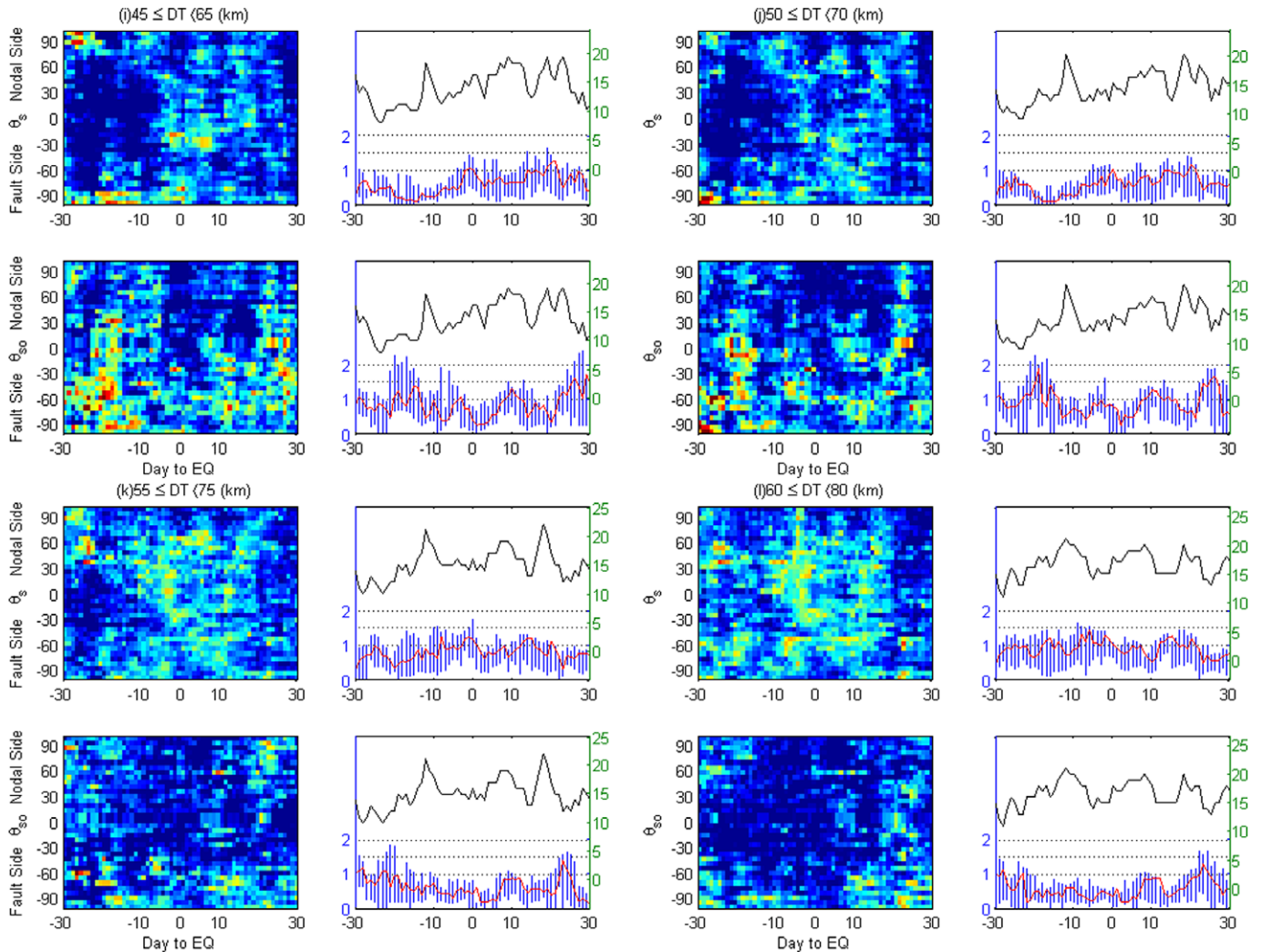


Fig. 2 (continued)

Observation and interpretation

Taiwan is located on the western side of the circum-pacific seismic zones and a complex interaction is formed by two collision zones (Ho, 1988). The northwest-moving Philippine Sea plate with a rate of 70 mm/year intensely impacts on the Eurasian plate, which results in occurrences of many large earthquakes in Taiwan. To further understand magnetic anomalies in this complex area, a 3-component fluxgate magnetometer station is set at the central Taiwan (120.47E, 23.56N) continuously recording the geomagnetic field variations with a sampling rate of 1 Hz. Meanwhile, the broadband array in Taiwan for seismology (BATS) routinely observes occurrences of earthquakes (Kao et al., 2002; Liang et al., 2003, 2004). During 2002–2005, 181 among 468 recorded earthquakes ($M_L \geq 4.0$ or $M_w \geq 3.3$) with the distance DT smaller than 120 km are selected. These earthquake fault plane solutions (Shearer, 1999) are employed in calculating the location of SMART, the fault and nodal lines (Fig. 1a).

Initially, we examine the background distribution of the normalized θ_{D_r} and θ_{D_m} (Fig. 1c). Due to the geomagnetic field with a small declination about -2° in Taiwan, θ_{D_r} is almost always facing on the north (Fig. 1c). The major difference between θ_{D_r} and θ_{D_m} is on the NE–SW and E–W trend that implies the locations of earthquakes being mainly at these two directions. Fig. 2 shows

the readjusted distribution of P_{θ_s} and $P_{\theta_{so}}$ and their bootstrap tests within a range of the distance DT from 0 to 80 km between -30 and 30 days of the onset of earthquakes. Because the insufficient events are occurrence with $DT \leq 15$ km, the bootstrap process cannot be carried out (Fig. 2a). P_{θ_s} do not directly point toward SMART due to a lack of distributions at the angle θ_s (see $\theta_s:0, -10$ to 10 days to EQ of the upper panels in Fig. 2a–j). Meanwhile, the bootstrap test shown in upper panels of Fig. 2b–f reveals that the 90CIs are significantly smaller than one 10 days before and after to earthquakes. This again suggests that the anomalous field does not point to SMART. With increase of DT , the 90CIs usually contain 1 during earthquake occurrence (Fig. 2g–j), which puts forward that the anomalous field is located within a range where DT is less than 70 km. On the other hand, P_{θ_s} in Fig. 2k and l are too scattered to identify the definitely pointed direction. Alternatively, $P_{\theta_{so}}$ are mainly distributed at θ_{so} which indicates that the field is pointed away from SMART (lower panels in Fig. 2). Fig. 2b–e illustrate that $P_{\theta_{so}}$ are centralized at θ_{so} 30 days before and 10 days after the earthquakes. It is worth to mention that the 90CIs in Fig. 2b–e are larger than 1 and the medians are significant to the background. $P_{\theta_{so}}$ and the 90CIs of Fig. 2f–i are generally close 1, while those of Fig. 2j–l become smaller than 1. These also indicate that the anomalous field can be observed as $DT \leq 70$ km. The results of

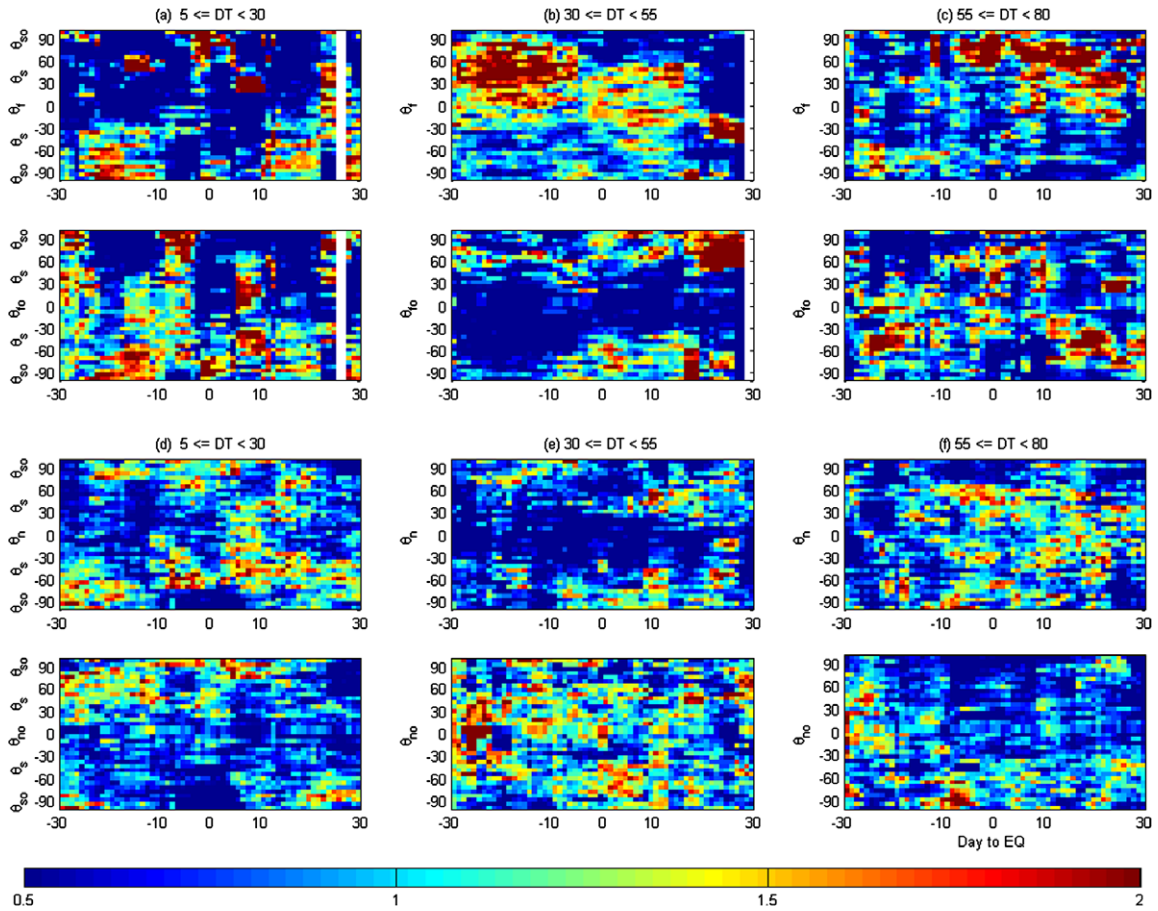


Fig. 3. The relationship between the distributions of P_a ($a = \theta_{fo}, \theta_f, \theta_n$ and θ_{no}) and DT 30 days before and after earthquakes. The azimuths follow a sequence of $\theta_f/\theta_n-\theta_s-\theta_{fo}/\theta_{no}-\theta_{so}$ for understanding the direction of the anomalous sources. The P_{of} or P_{ofo} ($DF \leq 15$ km) and P_{on} or P_{ono} ($DN \leq 15$ km) are, respectively, related with the distance of DT from 0 to 80 shown (a–c) and (d–f). The upper and bottom panels show the P_{of} or P_{on} and P_{ofo} or P_{ono} .

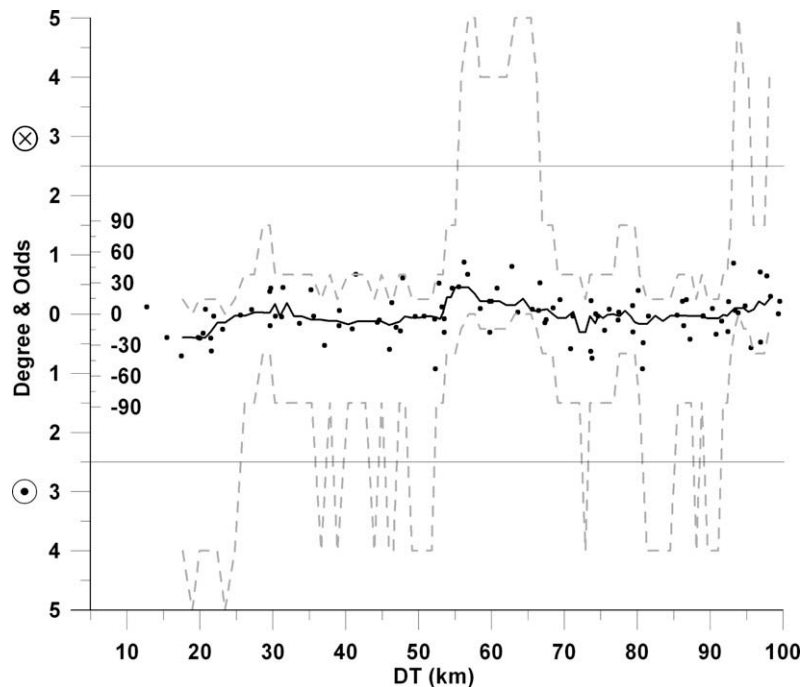


Fig. 4. The variations of θ_m and their odds results related to DT. The black plots denote the earthquake inclinations given by the median of the inclinations between -5 and 0 days to the earthquake. The shallow line (i.e. θ_m) is the running median of the earthquake inclinations with a window of five events. The dash line above (below) 0 is the odds obtained with the same window of five continuous earthquake inclinations for determining that the anomalies are significant or insignificant to the background. Note that the maximum of the odds is 5 , due to the window size.

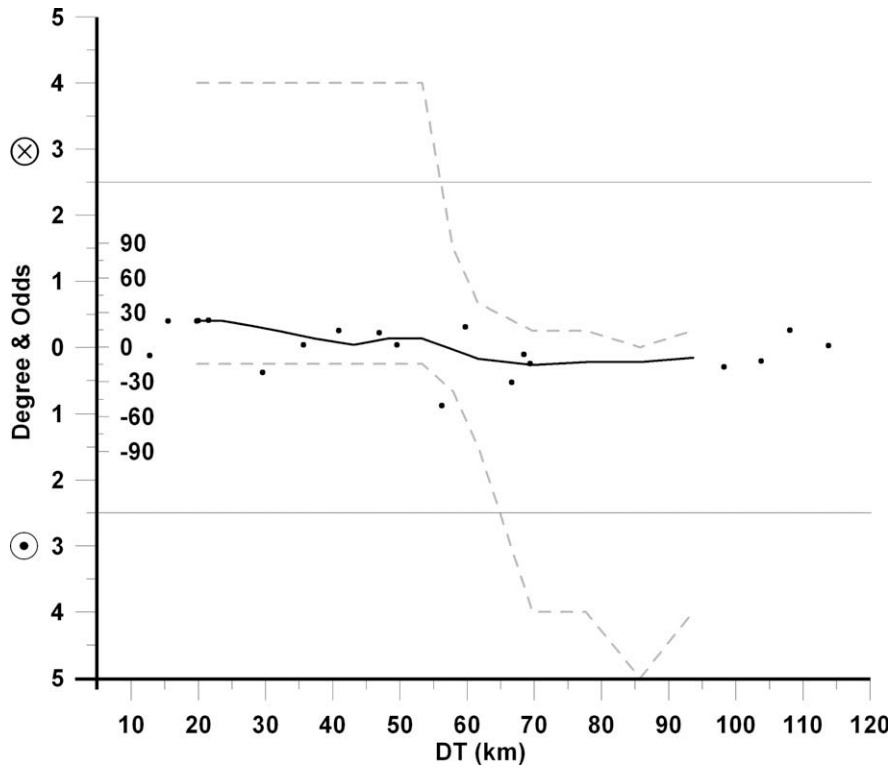


Fig. 5. The variations of θ_{l_m} along the fault lines and the odds related to DT. The black plots denote earthquake inclinations and the shallow line is the running mean within a window of five continuous events that are the same with Fig. 4. The dash lines are also the odds of the upward and downward inclinations.

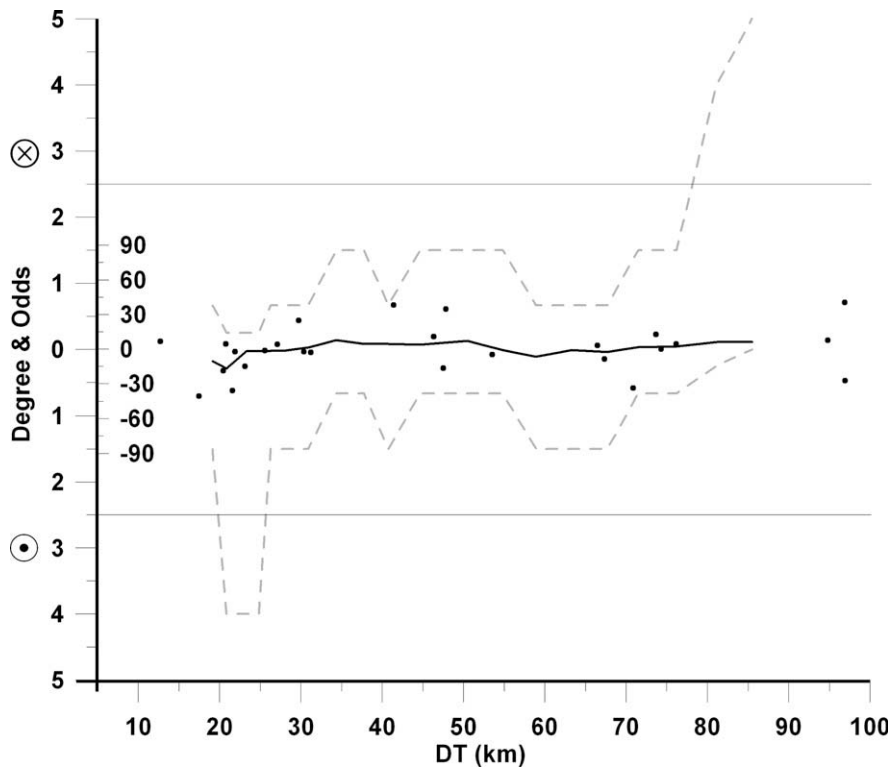


Fig. 6. The variations of θ_{l_m} along the nodal lines and the odds related to DT. Similarly, the black plots denote earthquake inclinations and the shallow line is the running mean within a window of five continuous events. The dash lines are also the odds of the upward and downward inclinations.

P_{θ_s} and/or $P_{\theta_{so}}$ in Fig. 2a–f shows that the anomalies are related to SMART together with the fault and nodal sides. Therefore, the

fault and nodal line directions, the other reference angles (θ_f , θ_n and θ_{no}), are taken into account in detail.

Table 1
The polarization of the geomagnetic field vs. DT

Unit (km)	$5 \leq DT < 30$	$30 \leq DT < 55$	$55 \leq DT < 80$
SMART, P_a	θ_{so}	θ_{so}	θ_{so}
θ_{I_m}	<0	~ 0	>0
Fault, P_a	Influenced by SMART	Influenced by SMART	θ_{fo}
θ_{I_m}	>0	~ 0	<0
Nodal, P_a	Influenced by SMART	Influenced by SMART	Influenced by SMART
θ_{I_m}	<0	~ 0	~ 0

Fig. 3 shows P_{of} , P_{of0} ($DF \leq 15$ km), P_{on} and P_{on0} ($DN \leq 15$ km) but sizes of the events along the fault and nodal lines are too small to run the bootstrap process. It is found that P_{of} and P_{of0} mainly direct to θ_s or θ_{so} (Fig. 3a and b). For $55 \leq DT \leq 80$ km, P_{of} are separated into two parts near θ_{so} (upper panel in Fig. 3c), and P_{of0} display that the polarizations are approximately opposite to the fault (lower panel in Fig. 3c). On the other hand, P_{on} and P_{on0} also imply effects from θ_s and/or θ_{so} directions and however they are

too scattered to determine their polarizations (Fig. 3d–f). In short, P_a except Fig. 3c are associated with θ_s or θ_{so} .

Variations of θ_{I_m} with DT are shown in Figs. 4 and 6. When the station is away from the fault and nodal lines, θ_{I_m} are upward where DT is smaller than 30 km (Fig. 4). For $30 \leq DT < 55$ km, the number of upward and downward θ_{I_m} are even which results the odds approaching 1. As $55 \leq DT < 70$ km, positive θ_{I_m} indicate the downward polarizations. It can be seen that the odds test and θ_{I_m} study yield a good agreement. Fig. 5 reveals θ_{I_m} along the fault line (i.e. $DF \leq 15$ km). Results show that θ_{I_m} are downward (upward) where DT is smaller (larger) than 55 km along the fault line. For the nodal lines, θ_{I_m} nearby SMART are upward and as $25 < DT < 80$ km become too scattered to identify polarization (Fig. 6).

Discussion and conclusions

There are in fact two methods to obtain the eigenvectors from an asymmetric matrix. One is a principal component analysis and

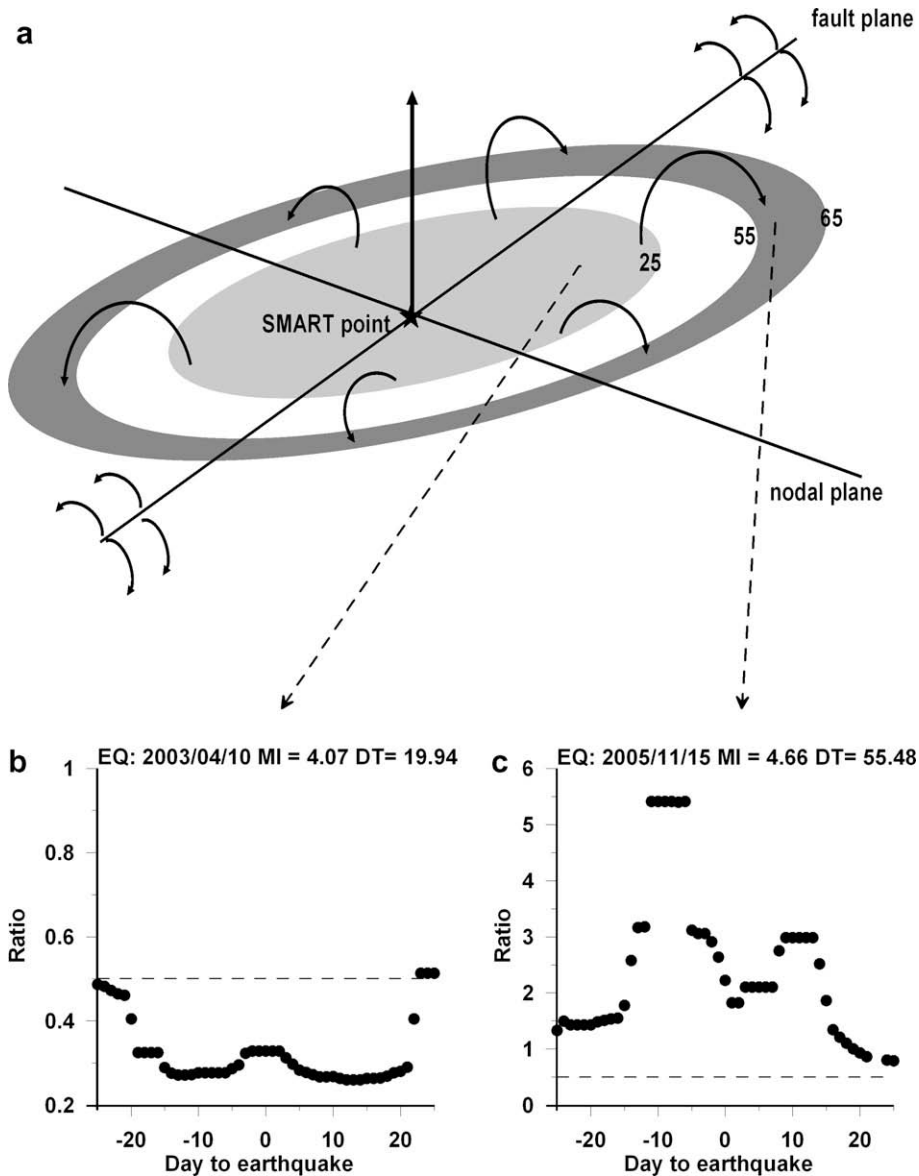


Fig. 7. A schematic showing the anomalous field produced an earthquake at the earth’s surface and the variations of the ratio in two true events. The arrows indicate the direction of the magnetic field (a). The numbers denote the distance of the DT (a). The plots are the ratios between the numbers of the negative and positive inclinations 5 days prior each day (b and c). The dash lines are the reference obtained by the ratio within the whole observation period (b and c).

the other is a SVD analysis. Using the principal component analysis, the mean subtracted data are employed to obtain a covariance matrix which is a measurement like a standard deviation to describe the variance between each two dimensions (Jolliffe, 2002). Actually, the magnetic data are vectors observed from the geomagnetic field. If the mean of the data is adjusted to be 0, the azimuths may be readjusted in an inverse direction. Such as a positive number in the data, which is smaller than data's mean, must be readjusted to be a negative one and results in the false appearance of the proportions in the inverse directions. Fig. 1c shows the comparison between the results obtained by these two different methods. The pattern obtained by the principal component analysis is mainly faced on the a degree of 45°, due to the increase of the inverse directions, and agrees with the above inference. By contrast, θD_r obtained by SVD points toward the north, which approaches the observed declination in Taiwan, is powerful evidence to explain that the SVD offers a good result and effectively reduces the disturbance to find the principal components in analyzing the vector data.

By combining the declinations (Figs. 2 and 3) and the inclinations (Figs. 4 and 6), the polarization of the anomalous field during earthquakes can be obtained. When the station is located in an area where DT is less than 30 km, θI_m and $P_{\theta so}$ are negative (Fig. 4) and gathered at θ_{so} (Fig. 2a–d), respectively. These show that the polarization is upward and away from SMART (Table 1). As $30 \leq DT \leq 55$ km, P_a weakly keep at θ_{so} (Fig. 2f–i) and θI_m approach 0, the horizontal direction (Fig. 4). For $55 \leq DT < 80$ km, P_a distributed at θ_{so} direction are smaller than background (Fig. 2k–l) and θI_m become downward (Fig. 4) in the exterior regions. Fig. 7a summarizes the above results that the magnetic lines are outward at the place near SMART and inward underground at the exterior area before earthquakes. These mean that the northern pole is close to the earth's surface and the southern one exists underground. Figs. 3c and 5 show that the polarizations along the fault are upward and directed away from the fault lines for $55 \leq DT < 80$ km (also see the sketch in Fig. 7a). This indicates that the anomalies are come from underground such as the place near SMART, which agrees with the observation obtained by Chen et al. (2008). Let's take two events (ML = 4.07 2003/4/10 and ML = 4.66 2005/11/15) in different DT to see inclination variations during earthquakes. Fig. 7b shows that the ratios (or the odds) indicates the upward inclinations appearance 20 days before and after the ML = 4.07 earthquake with DT = 19.94 km. On the other hand, the ratios of the ML = 4.66 event with DT = 55.48 km display that the positive inclinations increase 15 days before and return to the normal value 20 days after the earthquake (Fig. 7c). These two events are strong evidences for demonstrating the existence of the anomaly phenomena.

In conclusion, SMART is a useful reference for analyzing pre-earthquake geomagnetic anomalies. Results demonstrate the geomagnetic anomalous fields generally appear 10 days before the earthquakes. The anomalous fields are outward at the place near SMART but inward the earth's surface in the exterior area during the earthquake preparation period.

Acknowledgements

The authors wish to thank the Dr. B.S. Huang and Dr. W.T. Liang of Institute of Earth Sciences at Academia Sinica in Taiwan for providing the earthquake catalog with the fault plane solutions from Broadband Array in Taiwan for Seismology as well as the Central Weather Bureau for the geomagnetic data. We also thank two reviewers for helpful comments. This research was supported by the Taiwan Earthquake Research Center (TEC) funded through National Science Council (NSC) with grant number NSC97-2116-M-008-013. The TEC contribution number for this article is 00038.

References

- Agresti, A., 2002. *Categorical Data Analysis*, second ed. Wiley press.
- Bernardi, A., Fraser-Smith, A.C., McGill, P.R., Villard Jr., O.G., 1991. ULF magnetic field measurements near the epicenter of the Ms 7.1 Loma Prieta earthquake. *Phys. Earth Planet. Inter.* 68, 45–63.
- Blakeley, R.J., 1995. *Potential Theory in Gravity and Magnetic Applications*. Cambridge University Press. p. 441.
- Bhattacharyya, B.K., Leu, L.-K., 1975. Spectral analysis of gravity and magnetic anomalies due to two-dimensional structures. *Geophysics* 40, 993–1013.
- Chapman, S., Bartels, J., 1940. *Geomagnetism*. Clarendon Press, Oxford. p. 1049.
- Chen, C.H., Liu, J.Y., Lin, P.Y., Liang, W.T., Yen, H.Y., Hattori, K., Zeng, X., submitted for publication. Geomagnetism anomaly and earthquake location. *Tectonophysics*.
- Efron, B., 1987. Better bootstrap confidence interval. *J. Am. Stat. Assoc.* 82, 171–200.
- Fraser-Smith, A.C., Bernardi, A., McGill, P.R., Ladd, M.E., Helliwell, R.A., Villard Jr., O.G., 1990. Low-frequency magnetic field measurements near the epicenter of the Ms 7.1 Loma Prieta earthquake. *Geophys. Res. Lett.* 17, 1465–1468.
- Fraser-Smith, A.C., McGill, P.R., Helliwell, R.A., Villard Jr., O.G., 1994. Ultra-low frequency magnetic field measurements in southern California during the Northridge earthquake of 17 January 1994. *Geophys. Res. Lett.* 21, 2195–2198.
- Gotoh, K., Akinaga, Y., Hayakawa, M., Hattori, K., 2002. Principal component analysis of ULF geomagnetic data for Izu islands earthquakes in July 2000. *J. Atmos. Electr.* 22, 1–12.
- Hattori, K., Akinaga, Y., Hayakawa, M., Yumoto, K., Nagao, T., Uyeda, S., 2002. ULF magnetic anomaly preceding the 1997 Kagoshima earthquakes. *Seismo electromagnetics: lithosphere–atmosphere–ionosphere coupling*. In: Hayakawa, M., Molchanov, O.A. (Eds.), *Terra Scientific. Pub. Comp.*, Tokyo, pp. 19–28.
- Hattori, K., 2004. ULF geomagnetic changes associated with large earthquakes. *Terr. Atmos. Ocean. Sci.* 15, 329–360.
- Hattori, K., Takahashi, I., Yoshino, C., Isezaki, N., Iwasaki, H., Harada, M., Kawabata, K., Kopytenko, E., Kopytenko, Y., Maltsev, P., Korepanov, V., Molchanov, O., Hayakawa, M., Noda, Y., Nagao, T., Uyeda, S., 2004. ULF geomagnetic field measurements in Japan and some recent results associated with Iwateken Nairiku Hokubu earthquake in 1998. *Phys. Chem. Earth* 29, 481–494.
- Hattori, K., Serita, A., Gotoh, K., Yoshino, C., Harada, M., Isezaki, N., Hayakawa, M., 2004b. ULF geomagnetic anomaly associated with 2000 Izu islands earthquake swarm. *Jpn. Phys. Chem. Earth* 29, 425–435.
- Hattori, K., Serita, A., Yoshino, C., Hayakawa, M., Isezaki, N., 2006. Singular spectral analysis and principal component analysis for signal discrimination of ULF geomagnetic data associated with 2000 Izu island earthquake swarm. *Phys. Chem. Earth* 31, 281–291.
- Hayakawa, M., Fujinawa, Y. (Eds.), 1994. *Electromagnetic Phenomena Related to Earthquake Prediction*. Terra Scientific Pub. Comp., Tokyo. p. 677.
- Hayakawa, M. (Ed.), 1999. *Atmospheric and Ionospheric Electromagnetic Phenomena Associated with Earthquakes*. Terra Scientific. Pub. Comp., Tokyo, p. 996.
- Hayakawa, M., Itoh, T., Smirnova, N., 1999. Fractal analysis of ULF geomagnetic data associated with the Guam on August 8, 1993. *Geophys. Res. Lett.* 26, 2797–2800.
- Hayakawa, M., Itoh, T., Hattori, K., Yumoto, K., 2000. ULF electromagnetic precursors for an earthquake at Biak, Indonesia on February 17, 1996. *Geophys. Res. Lett.* 27, 1531–1534.
- Hayakawa, M., Molchanov, O.A. (Eds.), 2002. *Seismo Electromagnetics: Lithosphere–Atmosphere–Ionosphere Coupling*. Terra Scientific. Pub. Comp., Tokyo, p. 477.
- Ho, C.S., 1988. *An Introduction to the Geology of Taiwan*. Central Geological Survey, second ed. The Ministry of Economic Affairs, Taipei.
- Hsieh, S.H., Hu, C.C., 1972. Gravity and magnetic studies of Taiwan. *Petrol. Geol. Taiwan* 10, 283–321.
- Hu, C.C., Chen, W.S., 1986. Gravity and magnetic anomalies of eastern Taiwan. *Mem. Geol. Soc. China* 7, 341–352.
- Jolliffe, I.T., 2002. *Principal Component Analysis*, second ed. Springer, New York. p. 487.
- Kao, H., Liu, Y.H., Liang, W.T., Chen, W.P., 2002. Source parameters of regional earthquake in Taiwan: 1999–2000 including the Chi-Chi earthquake sequence. *Terr. Atmos. Ocean. Sci.* 13, 279–298.
- Kapicka, A., Hoffmann, V., Petrovsky, E., 2003. Pressure instability of magnetic susceptibility of pyrrhotite bearing rocks from the KTB borehole. *Stud. Geophys. Geod.* 47, 381–391.
- Kawate, R., Molchanov, O.A., Hayakawa, M., 1998. Ultra-low-frequency magnetic fields during the Guam earthquake of 8 August 1993 and their interpretation. *Phys. Earth Planet. Inter.* 105, 229–238.
- Kopytenko, Y.A., Matishvili, T.G., Voronov, P.M., Kopytenko, E.A., Molchanov, O.A., 1993. Detection of ultra-low-frequency emissions connected with the Spitak earthquake and its aftershock activity, based on geomagnetic pulsations data at Dusheti and Vardzia observatories. *Phys. Earth Planet. Inter.* 77, 85–95.
- Liang, W.T., Liu, Y.H., Kao, H., 2003. Source parameters of regional earthquake in Taiwan: January–December 2001. *Terr. Atmos. Ocean. Sci.* 14, 249–260.
- Liang, W.T., Liu, Y.H., Kao, H., 2004. Source parameters of regional earthquake in Taiwan: January–December 2002. *Terr. Atmos. Ocean. Sci.* 15, 727–741.
- Merzer, M., Klemperer, S.L., 1997. Modeling low-frequency magnetic-field precursor to the Loma Prieta earthquake with a precursory increase in fault-zone conductivity. *Pure Appl. Geophys.* 150, 217–248.
- Molchanov, O.A., Kopytenko, Y.A., Voronov, P.M., Kopytenko, E.A., Matishvili, T.G., Fraser-Smith, A.C., Bernardi, A., 1992. Results of ULF magnetic field

- measurements near the epicenters of the Spitak ($M_s = 6.9$) and Loma Prieta ($M_s = 7.1$) earthquakes: comparative analysis. *Geophys. Res. Lett.* 19, 1495–1498.
- Molchanov, O.A., Hayakawa, M., Rafalsky, V.A., 1995. Penetration characteristics of electromagnetic emissions from an underground seismic source into the atmosphere, ionosphere, and magnetosphere. *J. Geophys. Res.* 100, 1691–1712.
- Robert, D., Cain, J.C., 1975. The use of geomagnetic field models in magnetic surveys. *Geophysics* 40, 621–629.
- Shearer, P.M., 1999. *Introduction to Seismology*. Cambridge University Press, San Diego. p. 260.
- Telesca, L., Balasco, M., Colangelo, G., Lapenna, V., Macchiato, M., 2004. Investigating the multifractal properties of geoelectrical signals measured in southern Italy. *Phys. Chem. Earth* 29, 295–303.
- Telesca, L., Hattori, K., 2007. Non-uniform scaling behavior in ultra low frequency (ULF) earthquake-related geomagnetic signals. *Physica A* 384, 522–528.
- Yen, H.Y., Chen, C.H., Yeh, Y.H., Liu, J.Y., Lin, C.R., Tasi, Y.B., 2004. Geomagnetic fluctuations during the 1999 Chi-Chi earthquake in Taiwan. *Earth Planet. Sci. Lett.* 56, 39–45.
- Yen, H.Y., Chen, C.H., Hsieh, H.H., Lin, C.R., Yeh, Y.H., Tsai, Y.B., Liu, J.Y., Yu, G.K., Chen, Y.R., in press. Magnetic survey of Taiwan and its preliminary interpretations. *Terr. Atmos. Ocean. Sci.*